Crystal structure control of nanosized MnO_2 particles synthesized by a hydrothermal process using different Mn precursors

Young Ji Park*,**,‡, Yeon-Bin Choi*,***,‡, Sang Hyo Jeong*,‡, Tae Wook Kang*,‡, Byungseo Bae***,† and Sun Woog Kim*,†

*Advanced Materials Convergence R&D Division, Display Material Center, Korea Institute of Ceramic Engineering and Technology, Jinju 52851, Korea
**Department of Materials Science and Engineering, Gyeongsang National University, Jinju 52828, Korea
***Advanced Resources Team, Yeongwol Industrial Promotion Agency, Yeongwolgun 26240, Korea

Abstract Single-phase α-, β-, and γ-MnO_2 nanoparticles with high crystallinity were successfully synthesized by a hydrothermal process using different Mn precursors, such as $Mn(OAc)_2$, $MnSO_4$, $MnCl_2$, and $Mn(NO_3)_2$. The crystal structure and morphology of the MnO_2 particles could be effectively controlled by changing the Mn source. The use of $Mn(OAc)_2$ and $MnSO_4$ as precursors resulted in rod-shaped α- and β-MnO_2 particles, whereas $MnCl_2$ and $Mn(NO_3)_2$ yielded aggregated angular nanoparticles of γ-MnO_2. X-ray photoelectron spectroscopic analysis revealed that β-MnO_2 had a high ratio of Mn^{4+} and O_{latt} on the particle surface, whereas α- and γ-MnO_2 samples had a lower valence state of Mn, such as Mn^{3+} and Mn^{2+}, on the surface, and the ratio of O_{latt} was also relatively low.

Key words α-, β-, and γ-MnO_2, Acidity, Hydrothermal process, Particle morphology

1. Introduction

Lithium-ion batteries are generally utilized in electrical vehicles (EVs) and portable electronic products [1-3]. However, the low theoretical capacities of graphite anode materials in lithium-ion batteries hinder their further application in large-scale energy-storage devices [4]. In addition, lithium-ion batteries use flammable organic materials as electrolytes, which pose safety concerns, such as fire accidents. Therefore, the next generation of lithium-ion batteries with higher energy densities are required to meet the rapidly growing demand of the electrical vehicle market, and different cathode materials are sought to address this challenge. Among the various candidates, nanometer-sized transition-metal oxides have attracted significant attention because of their low cost, eco-friendliness, and high theoretical capacities in particular. Manganese dioxide (MnO_2), one of the transition-metal oxides, is an emerging electrode material because of its low toxicity, high specific capacity, and natural abundance [5-10]. Additionally, using MnO_2 as the cathode of lithium-ion batteries can result in reduced

cost. However, MnO_2-based cathode materials have significantly low electronic conductivity owing to suppressed electron transport in the MnO_2 lattice. During lithiation and delithiation processes, a large volume change occurs in MnO_2-based cathodes, resulting in severe electrode pulverization, serious safety problems, and rapid capacity loss during cycling.

To facilitate the utilization of MnO_2-based cathode materials, many strategies, such as the synthesis of various crystal phases of MnO_2 nanostructures or the introduction of heteroatoms, have been explored to increase their capacity and rate property. MnO_2 is generally known to have six different crystal structures: α-MnO_2 (2 × 2 tunnel or hollandite), β-MnO_2 (1 × 1 tunnel or pyrolusite), R-MnO_2 (2 × 1 tunnel or Ramsdellite), γ-MnO_2 (mix of 2 × 1 and 1 × 1 tunnels or nsutite), δ-MnO_2 (layered or birnessite), and λ-MnO_2 (three-dimensional pores or spinel). MnO_2 materials with different crystal structures have different ion selectivities or electron transport kinetics owing to their unique structural properties, such as the arrangement of atoms and the shape of pores or tunnels within the crystal structure. The electrochemical properties of a Li-ion battery using a MnO_2-based cathode depends strongly on the crystal structure and microstructure of the as-prepared MnO_2 material. Therefore, to enhance and control the perfor-

mance of the MnO_2-based Li-ion battery, it is necessary to develop an appropriate synthesis method for MnO_2 to control its crystal structure and microstructure.

Nanosized MnO_2 powders with different microstructures and crystal structures have been synthesized via various methods, such as co-precipitation [11], sol-gel synthesis [12], electrodeposition [13], and hydrothermal methods [14-16]. Among these, the hydrothermal method is the most widely used approach to prepare high-purity MnO_2 nanoparticles, because it allows easy control over the crystal structure and microstructure of MnO_2 [14-16]. Zhang et al. synthesized α-MnO_2 nanowires and β-MnO_2 microcrystals using a hydrothermal method, in which they used $KMnO_4$ and $Cr(NO_3)_3 \cdot 9H_2O$ as raw materials and controlled the redox reaction between MnO_4^- and Cr^{3+} to control the crystal structure and microstructure of MnO_2. Raheem et al. produced γ-MnO_2 with different particle morphologies using $NaClO_3$ as the oxidant and three different Mn sources ($MnSO_4 \cdot H_2O$, $MnCl_2 \cdot 4H_2O$, and $Mn(OAc)_2 \cdot 4H_2O$) to control the morphology of MnO_2 particles. Further, many studies have attempted to control the crystal structure and microstructure of MnO_2 particles using different oxidants, Mn sources, or salts.

In this study, we used the hydrothermal method to synthesize MnO_2 particles with a controlled crystal structure and microstructure using five different Mn sources. The crystal phase (α-, β-, or γ-MnO_2 phase) of the MnO_2 particles produced by our method depended on the type of Mn source. The mechanism underlying the change in the crystal structure and microstructure of MnO_2 according to the Mn source is discussed.

2. Experimental

2.1. Materials and synthesis of MnO_2

α-, β-, and γ-MnO_2 powders were synthesized by a hydrothermal method using different Mn precursors. Briefly, the Mn source, viz., 0.012 M of $Mn(OAc)_2 \cdot 4H_2O$ (98 %, Daejung), $MnSO_4 \cdot H_2O$ (98 %, Daejung), $MnCl_2 \cdot 4H_2O$ (98 %, Daejung), or $Mn(NO_3)_2 \cdot 4H_2O$ (98 %, Kanto Chemical Co., Inc.) was mixed with a 0.008 M $KMnO_4$ solution (Mn^{2+}:MnO^{4-} = 3:2 molar ratio) in 100 mL of deionized water. After being stirred for 2 h, the Mn^{2+}/MnO^{4-} solution was loaded into a Teflon container and placed in an autoclave, where a hydrothermal reaction was performed at 160°C for 2~48 h. After the reaction, the product was washed thrice

with deionized water and then dried at 100c+C for 24 h. The MnO_2 samples prepared using $Mn(OAc)_2 \cdot 4H_2O$, $MnSO_4 \cdot H_2O$, $MnCl_2 \cdot 4H_2O$, and $Mn(NO_3)_2 \cdot 4H_2O$ as precursors are denoted as sample_OAc, sample_SO4, sample_Cl2, and sample_NO3, respectively.

2.2. Characterization

The crystal structures of the different MnO_2 samples were identified via powder X-ray diffraction (XRD) analyses (Bruker D8 advance), and the crystallographic parameters were refined using the Rietveld method (RIETAN-FP) [17]. In the refinement, to determine the crystallographic parameters of the α-, β-, and γ-MnO_2 samples prepared in this study, the standard XRD patterns of α-, β-, and γ-MnO_2 samples from the inorganic crystal structure data (α-MnO_2: ICSD #20227; β-MnO_2: ICSD #643197; and γ-MnO_2: ICSD #653914) were used as the initial models. The microstructural analysis of the prepared materials was performed using a field-emission transmission electron microscope (FE-TEM, JEM 2100F; JEOL). Brunauer-Emmett-Teller (BET, TriStar 3020, Shimadzu) specific surface area was measured by performing nitrogen adsorption at −196°C. X-ray photoelectron spectroscopy (XPS; AXIS SUPRA) was performed at room temperature using Mg $K\alpha$ radiation (1,253.6 eV) without Ar-ion etching. The effect of charging on the binding energies was corrected by calibrating the peaks with respect to the C 1s peak at 284.6 eV. For XPS characterization, pelletized samples of 10 mm diameter were prepared from the powdered samples, and the pellets were placed in an ultrahigh vacuum chamber at 10^{-7} Pa.

3. Results and Discussion

To determine the crystal structures of the MnO_2 materials (sample_OAc, sample_SO4, sample_Cl2, and sample_NO3) prepared in this study using different Mn sources, viz., $Mn(OAc)_2 \cdot 4H_2O$, $MnSO_4 \cdot H_2O$, $MnCl_2 \cdot 4H_2O$, and $Mn(NO_3)_2 \cdot 4H_2O$, we conducted the Rietveld refinement of their XRD data. Figure 1 shows representative XRD patterns of α-, β-, and γ-MnO_2 powders obtained using the aforementioned Mn precursors. For the Rietveld refinement of these XRD patterns, we used the crystal structure data of α-, β-, and γ-MnO_2 from the inorganic crystal structure database (α-MnO_2: ICSD #20227; β-MnO_2: ICSD #643197; and γ-MnO_2: ICSD #653914) as preliminary models. The XRD patterns of
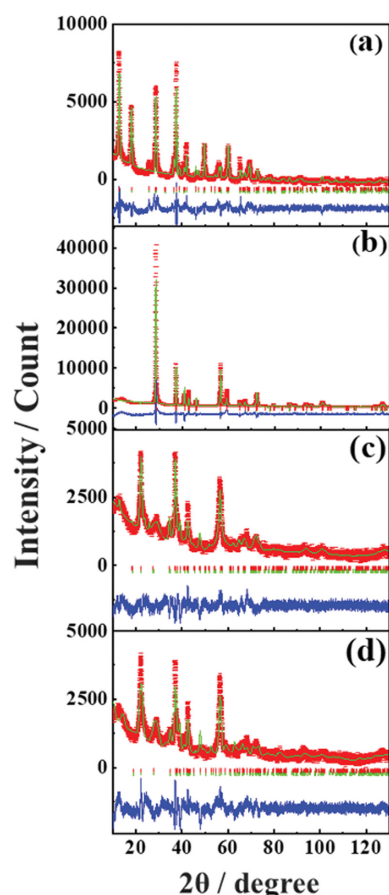
Fig. 1. Results of the Rietveld refinement of the X-ray powder diffraction patterns of the MnO$_2$ materials synthesized by a hydrothermal process at 160°C for 48 h using different Mn precursors: (a) sample_OAc, (b) sample_SO4, (c) sample_Cl2, and (d) sample_NO3. Red symbol: measured pattern, Green solid line: calculated pattern, Blue solid line: difference between the intensities of measured and calculated patterns.

the four samples could be indexed well with that of α-MnO$_2$ (ICSD #20227), β-MnO$_2$ (ICSD #643197), or

γ-MnO$_2$ (ICSD #653914), confirming the successful preparation of MnO$_2$ in three crystal structures. In addition, the MnO$_2$ samples with α- and β-type crystal structures were determined to have high crystallinity based on their narrow and intense peaks. The sample with the γ-MnO$_2$ structure had lower crystallinity than the other samples. As is well known, obtaining a single crystal phase of γ-MnO$_2$ is difficult, because γ-MnO$_2$ is generally formed by the irregular intergrowth of elements from ramsdellite and pyrolusite [18], usually resulting in a γ-MnO$_2$ powder of low crystallinity. The detailed crystallographic data and structural refinement parameters of the MnO$_2$ samples prepared in this study, as obtained by Rietveld refinement analysis, are listed in Table 1 and 2. The weighted profile R-factors of the MnO$_2$ samples, that is, the weighted-profile R-factor (R_{wp}), profile R-factor (R_p), and goodness-of-fit indicator (S) are 1.915~ 3.382 %, 1.449~2.110 %, and 1.6368~2.8957, respectively. These values indicate the phase purity of the as-prepared samples. The XRD pattern of sample_OAc agreed well with the α-type MnO$_2$ structure, and the refinement results yielded the following room-temperature parameters: a tetragonal system with the space group of I4/m (87); lattice parameters: a = 9.83391 nm, b = 9.83391 nm, and c = 2.85730 nm; and V = 0.2763 nm^3. Sample_SO4 adopted the β-type MnO$_2$ structure belonging to a tetragonal system with the space group of P42/mnm (136), and the lattice parameters calculated by Rietveld refinement are a = 4.40542 nm, b = 4.40542 nm, and c = 2.87381 nm; and V = 0.0557 nm^3. Further, sample_Cl2 and sample_NO3 adopted the γ-type MnO$_2$ structure, although a slight difference was observed in their lattice parameters. These two samples had an orthorhombic structure belonging to the space

Table 1

Crystallographic data and the refined lattice parameters of the MnO$_2$ samples prepared by a hydrothermal process at 160°C for 48 h using different Mn precursors ((a) sample_OAc, (b) sample_SO4, (c) sample_Cl2, and (d) sample_NO3), as obtained by the Rietveld refinement of the X-ray powder diffraction data collected at room temperature

	Sample			
	(a)	(b)	(c)	(d)
Crystal system	Tetragonal	Tetragonal	Orthorhombic	Orthorhombic
Space group	I 4/m	P42/mnm	Pnma	Pnma
a (nm)	9.83391	4.40542	9.62693	9.44894
b (nm)	9.83391	4.40542	2.79814	2.81793
c (nm)	2.85730	2.87381	4.38552	4.42020
R_{wp} (%)	2.546	3.382	1.915	2.303
R_p (%)	1.860	2.110	1.449	1.693
S (%)	2.0871	2.8957	1.6368	1.9509
d_1	0.4537	0.2494	0.7485	0.5272
d_2	0.3914	0.1556	0.7116	0.4861

Table 2
Refined structural parameters of MnO_2 prepared by a hydrothermal process at 160°C for 48 h using different Mn precursors ((a) sample_OAc, (b) sample_SO4, (c) sample_Cl2, and (d) sample_NO3), as obtained by the Rietveld refinement of the X-ray powder diffraction data collected at room temperature

Sample	Atom	Site	Occ.	x	y	z	Beq
(a)	Mn11	*8h*	1	0.35933	0.17223	0.00000	0.5
	O11	*8h*	1	0.12148	0.21099	0.00000	0.5
	O12	*8h*	1	0.18173	0.48725	0.00000	0.5
(b)	Mn11	*2a*	1	0.00000	0.00000	0.00000	0.5
	O11	*4f*	1	0.34485	0.34485	0.00000	0.5
(c)	Mn11	*4c*	1	0.12516	0.25000	-0.02169	0.5
	O11	*4c*	1	0.95887	0.25000	0.75791	0.5
	O12	*4c*	1	0.28242	0.25000	0.29906	0.5
(d)	Mn11	*4c*	1	0.12825	0.25000	-0.01243	0.5
	O11	*4c*	1	1.00153	0.25000	0.76202	0.5
	O12	*4c*	1	0.24163	0.25000	0.28342	1.0

Table 3
Mass fraction of the MnO_2 phases according to the Mn precursor ((a) sample_OAc, (b) sample_SO4, (c) sample_Cl2, and (d) sample_NO3), as obtained by the Rietveld refinement of the X-ray powder diffraction data collected at room temperature

Phases of MnO_2	The mass fraction of the MnO_2 phases			
	(a)	(b)	(c)	(d)
α-MnO_2	1.0000	0.0000	0.0000	0.0000
β-MnO_2	0.0000	1.0000	0.3098	0.4076
γ-MnO_2	0.0000	0.0000	0.6902	0.5924

group of Pnma (62) (see the other details in Table 1). To determine the ratios of α-, β-, and γ-MnO_2 phases in each sample prepared in this study, the mass fractions of the different MnO_2 phases in the samples were calculated by Rietveld refinement, and the results are shown in Table 3. Sample_OAc and sample_SO4 showed a single crystal phase of α-MnO_2 and β-MnO_2, respectively, without impurities; that is, they were monophasic materials with α-MnO_2 and β-MnO_2 structures, respectively. On the other hand, although the XRD patterns and Rietveld refinement profiles of sample_Cl2 and sample_NO3 agreed well with that of single-phase γ-MnO_2, an impurity phase corresponding to β-MnO_2 was also present, and the ratio of the γ- and β-MnO_2 phases was 69:31 in sample_Cl2 and 60:40 in sample_NO3. As mentioned above, the γ-MnO_2 crystal is known to form via the irregular intergrowth of elements from ramsdellite and pyrolusite, resulting in low crystallinity and the formation of a biphasic crystal.

Figure 2 presents the FE-TEM images of the samples prepared using different Mn precursors, viz., $Mn(OAc)_2 \cdot 4H_2O$, $MnSO_4 \cdot 4H_2O$, $MnCl_2 \cdot 4H_2O$, and $Mn(NO_3)_2 \cdot 4H_2O$. Sample_OAc and sample_SO4, which had α-type and β-type crystal structures, respectively, exhibited rod-like particle morphology. The length (L) and diameter (D) of the nanorods were determined to be 1.2 µm and 50~100 nm, respectively, for sample_OAc and 2 µm and 200~250 nm, respectively, for sample_SO4. The well-identified periodic lattice fringes of 7.05 Å (Fig. 2(b)) and 3.21 Å (Fig. 2(e)) correspond to the interplanar spacings of the (110) facets of α-MnO_2 and β-MnO_2 phases, respectively. These results indicate that α- and β-MnO_2 particles grow along the c-axis under the conditions of the hydrothermal synthesis. On the other hand, sample_Cl2 and sample_NO3, which have the γ-type crystal structure, showed plate-like particle morphology, and the particle sizes were determined to be approximately 200 nm. Although the lattice fringes of these MnO_2 samples with the γ-type crystal structure presented slight distortions owing to their low crystallinity and particle aggregation, these samples exhibited lattice fringe spacings of 2.29 and 4.01 Å (Fig. 2(h)) and 2.32 and 3.98 Å (Fig. 2(k)), respectively, which are in good agreement with the interplanar spacings of the (111) and (101) facets of γ-MnO_2, respectively.

The specific surface areas of the MnO_2 samples prepared in this study using different Mn precursors were analyzed by the BET method, which were 44 m^2/g for sample_OAc, 7 m^2/g for sample_SO4, 20 m^2/g for sample_Cl2, and 21 m^2/g for sample_NO3, respectively (Table 4). Figure 2 shows the schematics of the α-, β-, and γ-type MnO_2 crystal structures produced using VESTA based on the crystallographic data obtained by the Rietveld refinement analysis. Among the MnO_2 samples prepared in this study, sample_SO4 with the β-type MnO_2 crystal structure had a larger particle size, higher crystallinity, and a lower specific surface area
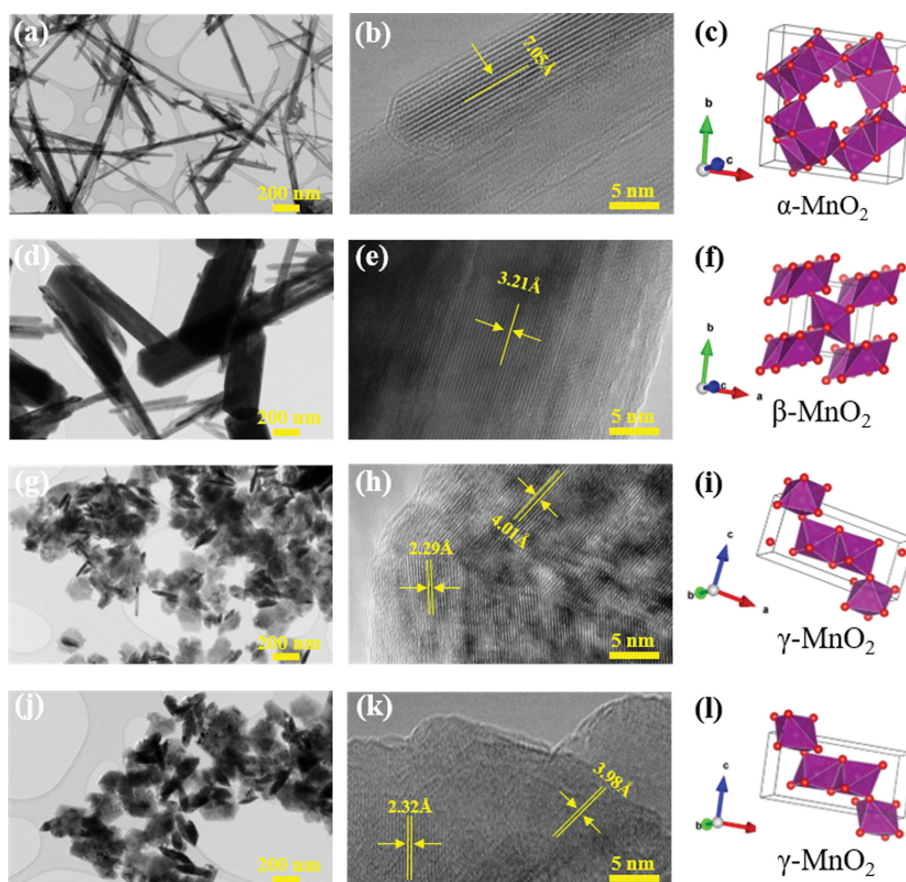
Fig. 2. FE-TEM images (left and center) and crystal structure diagrams (right) of (a~c) sample_OAc, (d~f) sample_SO4, (g~i) sample_Cl2, and (j~l) sample_NO3.

Table 4
The particle morphology, average particle size, and BET surface area of the MnO_2 according to Mn source; (a) sample_OAc, (b) sample_SO4, (c) sample_Cl2 and (d) sample_NO3 before hydrothermal reaction

Samples	Morphology	Average particle size	BET surface area
(a)	Rod	160 nm (D) 1,600 nm (L)	44 m^2/g
(b)	Rod	330 nm (D) 1,500nm(L)	7 m^2/g
(c)	Plank	270 nm (D)	20 m^2/g
(d)	Plank	330 nm (D)	21 m^2/g

than the other three samples (i.e., sample_OAc, sample_Cl2, and sample_(NO3). Further, sample_Cl2 and sample_NO3, which had the same γ-type MnO_2 crystal structure, exhibited a similar particle size, microstructure, crystallinity, and specific surface area. The differences in the crystal structures of MnO_2 prepared using different Mn precursors can be explained based on the difference in the local structure of each crystal type. According to their crystal structures, MnO_2 materials

have different tunnel structures formed by $[MnO_6]$ octahedrons. The α-, β-, and γ-type MnO_2 crystals synthesized in this study consist of $[2 \times 2]$, $[1 \times 1]$, and $[1 \times 2]$ tunnels, respectively, which are known to critically influence their crystallinity and specific surface area. The regular arrangement of the $[MnO_6]$ octahedrons in the crystal structure of MnO_2 results in the growth of the particles and improved crystallinity.

The foregoing results confirm that the crystal structure and morphology of MnO_2 nanomaterials can be successfully controlled by changing the Mn precursor (Mn base material). To analyze the changes in the crystal structure and particle morphology of the MnO_2 powder with a change in the Mn source, we investigated the effect of the anionic component of each Mn precursor (i.e., $Mn(OAc)_2 \cdot 4H_2O$, $MnSO_4 \cdot 4H_2O$, $MnCl_2 \cdot 4H_2O$, and $Mn(NO_3)_2 \cdot 4H_2O$) on the formation of MnO_2 particles with each crystal structure, that is, α-, β-, and γ-type MnO_2. The pH values of the precursor-only solutions were 7.06 for sample_OAc, 5.12 for sample_SO4, 5.03 for sample_Cl2, and 4.31 for sample_NO3, respectively. After mixing with $KMnO_4$, the pH values decreased

Table 5
The pH value of mixed solution according to Mn source; (a) sample_OAc, (b) sample_SO4, (c) sample_Cl2 and (d) sample_NO3 before hydrothermal reaction

Samples	pH value of (Precursor + D.I. Water) solution	pH value of (Precursor + KMnO$_4$ +D.I. Water) solution
(a)	7.06	3.84
(b)	5.12	1.40
(c)	5.03	1.08
(d)	4.31	1.03

Table 6
Chemical states of Mn and O in α-, β-, and γ-MnO$_2$ according to the Mn precursor: (a) sample_OAc, (b) sample_SO4, (c) sample_Cl2, and (d) sample_NO3 obtained from the XPS profiles of the Mn 2p$_{3/2}$ and O 1s core levels

Samples	(Mn^{2+} + Mn^{3+}) / Total Mn	O$_{ads}$ / O$_{latt}$
(a)	0.41	0.21
(b)	0.37	0.19
(c)	0.42	0.32
(d)	0.45	0.30

markedly to 3.84, 1.40, 1.08, and 1.03, respectively (Table 5). These differences in acidity are expected to play a critical role in the phase formation and crystallinity of MnO$_2$ during hydrothermal synthesis. In solution-phase chemical reactions, the solution pH is known to strongly influence the crystal structure, microstructure, and crystallinity of the final product. In addition to acidity, the counter-anions can also affect the hydrothermal reaction, as previous studies have shown that different anionic species can modify hydrolysis and selectively adsorb on specific crystal facets, thereby influencing nucleation and growth behavior [19]. Although the γ-type MnO$_2$ structure has lower thermodynamic stability than the α- and β-type MnO$_2$ structures, the γ-type structure is more easily formed than the other structures

at a low pH, possibly due to the dissolution and subsequent recrystallization of the Mn precursor in the low-pH solution. This phenomenon has already been documented in some previous reports [20,21]; it has been reported that tetragonal BiVO$_4$, which has a relatively low thermodynamic stability than monoclinic BiVO$_4$, is kinetically more feasible at a relatively low pH of the precursor solution.

To determine the oxidation states of Mn and O ions in the α-, β-, and γ-MnO$_2$ samples according to the Mn precursor used in this study, XPS analysis was carried out in the binding energy range of 0~1,200 eV, and the results are shown in Fig. 3 and Table 6. In the Mn 2p$_{3/2}$ spectra, the peaks appearing at 642.7, 641.7, and 640.4 eV can be attributed to Mn^{4+}, Mn^{3+}, and Mn^{2+}, respectively (Fig. 3a) [22-24]. As shown in Table 6, the proportion of low-valence Mn (Mn^{2+} + Mn^{3+}) to total Mn, which is an indicator of surface oxygen vacancies, followed the order of γ-MnO$_2$ (sample_Cl2) (0.45) > γ-MnO$_2$ (sample_NO3) (0.42) > α-MnO$_2$ (sample_OAc) (0.41) > β-MnO$_2$ (sample_SO4) (0.37). Thus, the proportion of low-valence Mn on the surface of β-MnO$_2$ particles was considerably low. However, α- and γ-MnO$_2$ particles tended to have more Mn^{3+} and Mn^{2+} on the surface owing to their intrinsic crystal defects. These results suggest that the existence of a large population of low-valence Mn species on the particle surface would promote the dissociation and activation of circumambient oxygen atoms, because Mn^{2+}-O and Mn^{3+}-O bonds are weaker than the Mn^{4+}-O bonds [25]. In the XPS O 1s profiles of the samples shown in Fig. 3(b), the peaks at 532.0, 531.0, and 529.6 eV can be assigned to surface hydroxyl oxygen, surface adsorbed oxygen (O$_{ads}$), and lattice oxygen (O$_{latt}$), respectively [23]. Among the different samples, γ-MnO$_2$ showed the largest O$_{ads}$/O$_{latt}$ ratio (Table 6). The O peaks of β-MnO$_2$ shifted slightly toward the lower binding energy region, indicating that the electron cloud density of O was greater, which may result in the neutralization of the surface oxygen species in this sample [24].
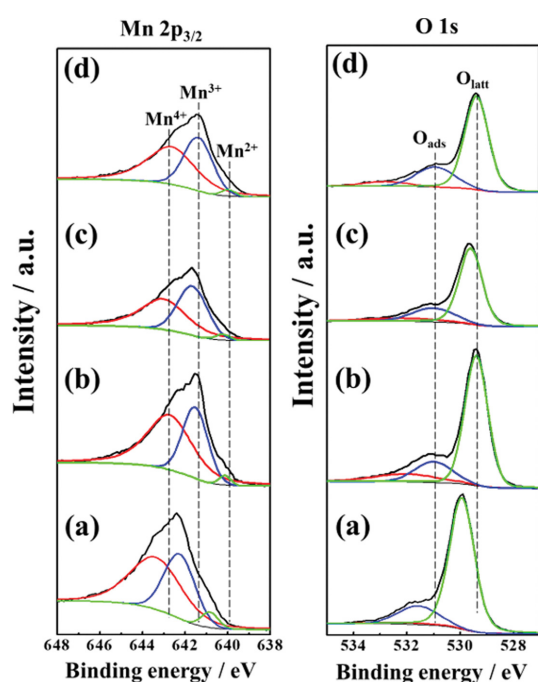

Fig. 3. XPS profiles of the Mn 2p$_{3/2}$ and O 1s core levels of MnO$_2$ according to the Mn source: (a) sample_OAc, (b) sample_SO4, (c) sample_Cl2, and (d) sample_NO3.

4. Conclusions

Single-phase particles of α-, β-, and γ-MnO₂ were successfully synthesized by a hydrothermal process using different Mn sources. The results indicated that the particle morphology and crystal structure of MnO₂ could be effectively controlled by changing the Mn precursor. The sample synthesized using Mn(OAc)₂·4H₂O (sample_OAc) adopted a single-phase tetragonal structure of α-MnO₂ with the space group of I4/m(87), and it was composed of nanorod-like particles with 1.2 μm length and 50~100 nm diameter. The sample synthesized using MnSO₄·H₂O (sample_SO4) was also of a single phase, and it adopted the tetragonal β-MnO₂ structure with the space group of P42/mnm (136) and consisted of micro-rod-like particles of 2 μm length and 200~250 nm diameter. In the cases of the samples prepared using MnCl₂·4H₂O (sample_Cl2) and Mn(NO₃)₂·4H₂O (sample_NO3), a single phase of orthorhombic γ-MnO₂ with the space group of Pnma (62) was formed, and a small impurity phase was observed. These two samples were composed of aggregated angular nanoparticles of ~200 nm diameter. The proportions of high-valence Mn^{4+} and O_{latt} were relatively high on the β-MnO₂ surface, corresponding to its stable crystal phase. On the other hand, the α- and γ-MnO₂ materials tended to have lower-valence Mn^{3+} and Mn^{2+} species, along with a low proportion of O_{latt}, on their surfaces because of their intrinsic crystal defects and oxygen vacancies.

Conflicts of Interest

The authors declare no conflict of interest.

Acknowledgements

References

[1] X. Guo, J. Han, L. Zhang, P. Liu, A. Hirata, L. Chen, T. Fujita and M. Chen, "Facile preparation of 1D α-MnO₂ as anode materials for Li-ion batteries", Nanoscale 7 (2015) 15111.

[2] Y.C. Tsai, C.T. Kuo, S.F. Liu, Y.T. Lee and T.R. Yew, "Effect of different electrolytes on MnO₂ anodes in lithium-ion batteries", J. Phys. Chem. C 125 (2021) 1221.

[3] E.C. Evarts, "Lithium batteries: To the limits of lithium", Nature 526 (2015) S93.

[4] N. Zhang, G. Guo, B. He, J. Zhu, J. Wu and J. Qiu, "Synthesis and research of MnO₂-NiO composite as lithium-ion battery anode using spent Zn-Mn batteries as manganese source", J. Alloys Compd. 838 (2020) 155578.

[5] X. Gu, J. Yue, L. Li, H. Xue, J. Yang and X. Zhao, "General synthesis of MnOx (MnO₂, Mn₂O₃, Mn₃O₄, MnO) hierarchical microspheres as lithium-ion battery anodes", Electrochim. Acta 184 (2015) 250.

[6] P. Poizot, S. Laruelle, S. Grugeon, L. Dupont and J. Tarascon, "Searching for new anode materials for the Li-ion technology: time to deviate from the usual path", J. Power Sources 97-98 (2001) 235.

[7] X. Gao, J. Bao, G. Pan, H. Zhu, P. Huang, F. Wu and D. Song, "Preparation and electrochemical performance of polycrystalline and single crystalline CuO nanorods as anode materials for Li-ion batteries", J. Phys. Chem. B 108 (2004) 5547.

[8] Y.M. Kang, M.S. Song, J.H. Kim, H.S. Kim, M.S. Park, J.Y. Lee, H.K. Liu and S. Dou, "A study on the charge-discharge mechanism of Co₃O₄ as an anode for the Li-ion secondary battery", Electrochim. Acta 50 (2005) 3667.

[9] M. Reddy, G. Subba Rao and B. Chowdari, "Metal oxides and oxysalts as anode materials for Li-Ion batteries", Chem. Rev. 113 (2013) 5364.

[10] X.L. Huang, R.Z. Wang, D. Xu, Z.L. Wang, H.G. Wang, J.J. Xu, Z. Wu, Q.C. Liu, Y. Zhang and X.B. Zhang, "Homogeneous CoO on graphene for binder-free and ultralong-life lithium ion batteries", Adv. Funct. Mater. 23 (2013) 4345.

[11] J. Zhang, J. Du, H. Wang, J. Wang, Z. Qu and L. Jia, "Facile preparation of Mn₃O₄ hausmannite nanoplates from a new octahedral manganese(III) Schiff-base complex", Mater. Lett. 65 (2011) 2565.

[12] A. Vazquez-Olmos, R. Rodon, G. Rodriguez-Gattorno, M. Mata-Zamora, F. Morales-Leal and A. Fernandez-Osorio, "Experimental analysis of floc size distributions in a 1-L jar under different hydrodynamics and physicochemical conditions", J. Colloid Interface Sci. 291 (2005) 175.

[13] K. Sankar, D. Kalpana and R. Selvan, "Electrochemical properties of microwave-assisted reflux-synthesized Mn₃O₄ nanoparticles in different electrolytes for supercapacitor applications", J. Appl. Electro. Chem. 42 (2012) 463.

[14] L. Liu, H. Yang, J. Wei and Y. Yang, "Controllable synthesis of monodisperse Mn₃O₄ and Mn₂O₃ nanoparticles via chemical precipitation approach", Mater. Lett. 65 (2011) 694.

[15] Y. Tan, L. Meng, Q. Peng and Y. Li, "One-dimensional single-crystalline Mn₃O₄ nanostructures with tunable length and magnetic properties of Mn₃O₄ nanowires",

Chem. Commun. 47 (2011) 1172.

[16] S. Ashoka, G. Nagaraju and G. Chandrappa, "Reduction of $KMnO_4$ to Mn_3O_4 via hydrothermal process", Mater. Lett. 64 (2010) 2538.

[17] F. Izumi and K. Momma, "Three-dimensional visualization in powder diffraction", Solid State Phenom. 130 (2007) 15.

[18] Z.H. Raheem and A.M. Sammarraie, "Hydrothermal synthesis of γ-MnO_2 nanostructures with different morphologies using different Mn^{2+} precursors", Sys Rev Pharm. 11 (2020) 453.

[19] S.N. Matussin, A. Rahman and M.M. Khan, "Role of anions in the synthesis and crystal growth of selected semiconductors", Front. Chem. 10 (2022) 881518.

[20] C.X. Liu, L.Z. Zhang and L. Xiang, "Effect of pH on formation of γ-MnO_2 from Zn bearing $MnSO_4$ solution", J. Phys. Conf. Ser. 339 (2012) 012009.

[21] L.I. Hill, A. Verbaere and D. Guyomard, "MnO_2 (α-, β-, γ-) compounds prepared by hydrothermal-electrochemi-cal synthesis: characterization, morphology, and lithium insertion behavior", J. Power Sources 119 (2003) 226.

[22] Y. Meng, K. Zhao, Z. Zhang, P. Gao, J. Yuan, T. Cai, Q. Tong, G. Huang and D. He, "Effects of crystal structure on the activity of MnO_2 nanorods oxidase mimics", Nano Research 13 (2020) 709.

[23] W. Yanga, Z. Sua, Z. Xua, W. Yanga, Y. Peng and J. Lia, "Comparative study of α-, β-, γ- and δ-MnO_2 on toluene oxidation: Oxygen vacancies and reaction intermediates", Appl. Catal. B: Environ. 260 (2020) 118150.

[24] J. Zhang, Y. Li, L. Wang, C. Zhang and H. He, "Catalytic oxidation of formaldehyde over manganese oxides with different crystal structures", Catal. Sci. Technol. 5 (2015) 2305.

[25] H. Zheng, M. Modibedi, M. Mathe and K. Ozoemena, "The thermal effect on the catalytic activity of MnO_2 (α, β, and γ) for oxygen reduction reaction", Mater. Today Proc. 4 (2017) 11624.